AIAA AVIATION Forum
5-9 June 2017, Denver, Colorado
35th AIAA Applied Aerodynamics Conference

10.2514/6.2017-3918

Multiple Fidelity Modeling of Interactional Aerodynamics

Asitav Mishra,* Behdad Davoudi, † Karthik Duraisamy,‡
University of Michigan, Department of Aerospace Engineering, Ann Arbor, MI

The interaction of trailing vortices with lifting surfaces is investigated using two levels of modeling fidelity. A RANS-based computational fluid dynamics solver is considered as the high-fidelity computational model and a vortex panel method with a propeller model is considered as the low-fidelity computational model. The high-fidelity model is first validated against available experimental data obtained from the interaction of a trailing vortex generated by an upstream wing with a downstream wing. The ability of the models to represent the development of the vortex wake and integrated loads is assessed for a number of parametric configurations, including a case in which the vortex core directly impacts the wing surface. Following this, configurations of an isolated propeller and a wing-mounted propeller are studied. In all of these cases, the high-fidelity model is effective in predicting the details of the flow and integrated airloads. The low-fidelity model, while less accurate is shown to successfully represent integrated quantities well at orders of magnitude less cost than the high-fidelity model, justifying its role as a viable tool in design and trajectory planning applications.

I. Introduction

New mission profiles and performance requirements are driving the aerospace community towards novel designs of both unmanned and manned aircraft. As an example, Distributed propulsion (DP) has recently been identified as a 'disruptive technology' by NASA that can positively impact evolutionary aircraft designs. DP can enable novel aircraft designs, for both commercial and unmanned air vehicles, with performance advantages, scaling and efficient vertical take-off and landing (VTOL) characteristics. Recently, significant advances have been made in this regard by NASA in the form of LEAPTech [1] and GL-10 [2].

The versatility and improved performance of these concepts, however, comes at the expense of increased complexity. For example, the GL-10 flight path [2] includes both hover and cruise mode and the aircraft experiences a complex flight transition phase between hover and cruise flight modes. This requires an efficient optimization strategy for flight trajectory control in conjunction with optimized aerodynamic design for the complex propulsion interactions.

In these problems, it is critical to accurately model the evolution of the rotor wake and its interaction with lifting surfaces. Accurate resolution of the near-blade affects the accuracy of the prediction of the blade airloads, vibratory loads and aeroacoustic signatures. The interaction of the trailing vortex system with a lifting surface affects the blade loading and can impact blade stall and loading noise.

State-of-the-art RANS-based CFD solvers - with a careful consideration of numerical resolution are capable of accurately modeling the interactional flowfield. However, the high computational costs rule out the use of highly resolved CFD computations at the design stage. In this context, lower-fidelity vortex methods present an effective and efficient alternative class of methods to CFD in capturing essential features of the interaction. Another area of need for low-fidelity methods is in trajectory and mission planning, an exercise in which the aerodynamic model may be executed 100s of thousands of times.

In many situations, (hovering rotors and propellers, especially) vortical interactions with lifting surfaces is dominantly perpendicular in nature. This interaction can have a significant consequence on the blade loading, and on overall performance. A natural choice to mimic this behavior is to use a simplified fixed-wing model which would provide deeper understanding of its flow physics. In literature, only a limited number of experimental efforts exist [3, 4, 5] that study wing-vortex interaction. Komerath et al. [6] in their review paper have emphasized on further fundamental experimental studies to understand rotor wake. Recently, experimental studies by Bhagwat et al. [7] and Ramasamy et al. [8] attempt to understand the fundamental nature of the interaction. Detailed measurements have been performed to study the loading and wake structure of a wing-vortex interaction using a combination of extensive surface pressure, balance loads, and 3-component PIV measurements. These experiments would provide data of adequate quality to improve existing vortex models besides enabling validations of computational simulations. Their recently conducted

*Post Doctoral Scholar
†PhD Candidate
‡Associate Professor, AIAA Member

first phase of measurements provides sufficient data on spanwise loads and wake behavior for a range of wing-vortex interaction conditions.

The goal of the present work is thus to study the predictive capabilities of both CFD-based high-fidelity models as well as vortex-based low-fidelity models. The CFD model is first validated against two sets of available experimental data, namely, for i) a parametric set of fixed wing-vortex interaction case, studied by Bhagwat et al. [7] and, ii) propeller and propeller-wing interaction cases studied by Samuelsson [9, 10]. Then, the low-fidelity model capabilities are be evaluated against the CFD predictions and experimental measurements, where available.

II. Methodology

A. High-fidelity Model: Overset Computational Fluid Dynamics Solver

The CFD solver used in the present work is the overset structured mesh solver OVERTURNS [11, 12, 13, 14] (OVERset Transonic Unsteady Rotor Navier-Stokes). The compressible Reynolds Averaged Navier–Stokes equations are solved with a Spalart-Allmaras model [15] for closure. Time integration is performed using second order backward difference method using Lower-Upper Symmetric Gauss Seidel (LUSGS). Newton sub-iterations are used to remove factorization errors and recover time accuracy for unsteady computations. The inviscid fluxes are calculated using a third order accurate upwind scheme that uses Roe's flux differencing [16], while the viscous fluxes are computed using second order central differencing. The solver uses an overset mesh system for efficient mesh resolution. In this arrangement, the body-fitted blade meshes are embedded inside a Cartesian off-body mesh to capture the entire wing-wake aerodynamics. The solver uses a novel Implicit Hole-Cutting (IHC) technique[17], which has been efficiently used in several computational studies on complex rotary wing flows [18, 19, 13, 14]

B. Low-fidelity Model: Vortex Panel Method

The low-fidelity model uses vortex panels [20] to analyze forces exerted on a lifting surface. The lifting surface is partitioned into vortex panels (of strength Γ_i) in the stream- and span-wise directions and bound vortices are placed at the quarter-chord location of each panel. The wake is considered as an extension of the TE panel with the same vorticity magnitude and ideally extends to infinity. To determine the strength of bound vortices, the induced velocity from all of the panels (including the self-induced effects), the wake and any other source of induced velocity at the control points are considered. A linear system is formed by enforcing flow tangency at the control points.

From potential flow theory, the pressure differential for each panel is obtained using:

$$\Delta P_{ij} = \rho\{[U(t)+u_w, V(t)+v_w, W(t)+w_w]_{ij}.\tau_i \frac{\Gamma_{i,j}-\Gamma_{i-1,j}}{\Delta c_{ij}} + [U(t)+u_w, V(t)+v_w, W(t)+w_w]_{ij}.\tau_j \frac{\Gamma_{i,j}-\Gamma_{i,j-1}}{\Delta b_{ij}} + \frac{\partial}{\partial t}\Gamma_{ij}\} \quad (1)$$

where, U, V and W are flow velocities in the three directions. The indices i and j are in stream- and span-wise directions respectively. Δc_{ij} and Δb_{ij} are the stream- and span-wise lengths of a panel at i,j locations and u_w, v_w and w_w are the induced velocity by the wake on the panel. τ_j and τ_j are the tangential vectors to the panel in i and j directions, respectively.

It is noted that for the panels at the leading edge, $\Gamma_{i,j}$ is substituted for $\Gamma_{i,j} - \Gamma_{i-1,j}$. Also, for the panels at the tip, $\Gamma_{i,j} - \Gamma_{i,j-1}$ is assumed to be zero. Several validation and verification studies have been conducted. Validations and comparisons with CFD data and experiment are presented in later sections.

1. Propeller Aerodynamic Model

To efficiently represent the the propeller blade, a model from helicopter aerodynamic theory [21] called extended blade element theory is adapted. The sectional lift coefficient c_l is simply found by estimating the 2D lift curve slope c_{l_α} and the inflow angle as:

$$c_l = c_{l_\alpha}(\theta - \phi) \quad (2)$$

where the inflow angle is obtained as $\phi(r) = \lambda(r)/r$ and θ is the blade pitch angle. The process of finding the inflow coefficient λ requires an iterative method that also takes into account the lift loss at the root and tip of the blade. This involves solving the following set of equations:

$$\lambda(r,J) = \sqrt{(\frac{\sigma c_{l_\alpha}}{16F} - \frac{J}{2})^2 + \frac{\sigma c_{l_\alpha}}{8F}\theta r} - (\frac{\sigma c_{l_\alpha}}{16F} - \frac{J}{2}) \tag{3}$$

$$F = \frac{4}{\pi^2}\cos^{-1}(\exp(-f_{root}))\cos^{-1}(\exp(-f_{tip})) \tag{4}$$

where J is the advance ratio, σ is the blade solidity, $f_{root} = \frac{N_b}{2}\frac{r}{(1-r)\phi}$ and $f_{tip} = \frac{N_b}{2}\frac{(1-r)}{(r\phi}$). Function F is referred to as Prandtl's loss function.

To analyze the axial and swirl velocity behind the propeller, a slip-stream theory model is adapted from Ref. [22] and Ref. [23]. This model requires the vorticity magnitude on the blade, and it is a common practice to obtain it using experiment or pre-defined empirical functions. We, however, used the extended blade element theory to calculate the lift and convert it to vorticity using Kutta-Joukowski theorem as follows:

$$\Gamma = \frac{1}{2}\Omega r c c_l \tag{5}$$

Given the vorticity, one can estimate axial and swirl velocities of a propeller subjet to free stream U_∞ as:

$$V_{swirl}(r) = \frac{N_b\Gamma(r)}{2\pi r} \tag{6}$$

$$V_{axial}(r) = U_\infty + \frac{N_b n\Gamma(r)}{4\pi U_\infty}\left(1 + \frac{x}{\sqrt{r^2+x^2}}\right) \tag{7}$$

where x is the distance from the propeller plane, N_b is the number of blades and n is the propeller rotation rate in revolutions per second. It is noted that at $x = \infty$, both axial and swirl velocities eventually attain twice the value of that at the propeller plane, which is in agreement with the conventional momentum theory.

Using the velocity information behind the propeller, we can evaluate the interaction between the propeller and a fixed wing by combining the propeller model and the vortex panel code developed earlier. A comparison between the predicted interaction effects using CFD and current analytical model will be presented in later sections.

III. Vortex-Wing Interaction

A. Fixed wing-Vortex Interaction Test Configuration

The test was conducted in the 7 by 10-ft wind tunnel at Ames Research Center for a range of tunnel speeds up to about V_∞ = 242 ft/s (q_∞ = 70 psf or $M_\infty = 0.21695$). Measurements were performed on a pressure instrumented NACA0015 12-inch chord wing. The perpendicular vortex wake was generated by a NACA0015 18-inch chord wing (VG). Both the wings are rectangular, straight and untwisted. The maximum chord Reynolds numbers are 1.5×10^6 and 2.2×10^6 for the wing and the VG, respectively. The VG was placed vertically in front of the wing at several locations varying in stream wise, span-wise and vertical positions with respect to the wing. More details can be found in Bhagwat et al. [7]. Pressure measurements were obtained for each of these wings with (and without) VG configurations at several span wise stations on the wing to study the effects of vortex wake on the wing loading.

One of the main goals of the experiment was to measure the wing-vortex wake system and its affect on the wing loading. Therefore, velocity field measurements behind the wing-vortex generator were made using stereoscopic particle image velocimetry (PIV). The velocity field measurements were obtained on a plane normal to the tunnel flow over 3.5×2 ft.

B. High-fidelity model details:

The near-body wing and vortex generator (VG) flow fields are modeled using C–O type body confirming meshes. Wing mesh has $267 \times 185 \times 101$ points (in chordwise, spanwise and normal directions, respectively) and VG mesh has $267 \times 145 \times 101$ points. The blade surface spacing in the normal direction is 5×10^{-6} chords (required for viscous calculations) and the mesh outer boundary is at a distance of two chords away from the blade surface. The entire rotor blade-wake system is modeled by embedding both the blade meshes in a Cartesian background (wind tunnel) mesh with $240 \times 201 \times 201$ points — see Fig. 1.

There are a few details in the experiment that require careful adjustments so that the simulation accurately captures the physics of the problem. The following considerations were made to achieve reasonable comparison with the experimental data.

1. The side walls in the background mesh were treated as viscous walls.

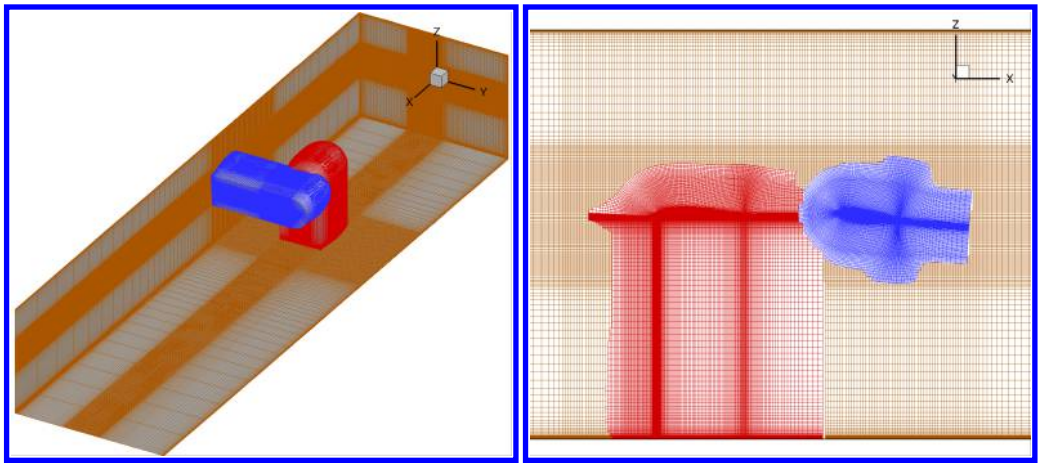

(a) Computational domain (b) Hole cut mesh system

Figure 1. Overset mesh system of wing-vortex interaction

2. The velocity inlet magnitude was modified to accommodate the blockage effects of the objects in the wind tunnel.

C. Low-fidelity model details

In the high-fidelity model, the flow corresponding to the vortex generator is resolved. In the low fidelity model, a Lamb-Oseen vortex was used to model the VG tip vortex that generates the following velocity field:

$$V_\theta(r,\theta) = \frac{\Gamma_{VG}}{2\pi r}\left(1 - \exp(-\frac{r^2}{r_c^2})\right) \tag{8}$$

Following Ref. [24], a core radius of 1.5" for VG tip vortex was used. The vorticity magnitude Γ_{VG} is, according to Betz's roll-up theory [25], the maximum vorticity at the root of the VG that can be obtained by running the panel code for the VG alone. Having obtained the velocity field generated by tip vortex of the VG, one can find the induced velocity on the wing, and thus obtain the resultant lift distribution.

D. Wing-alone Case

An isolated wing was considered first and predictions are compared against the experimental airload data. The wing angle of attack (α_w) was set to 7 degrees in this case. As observed in Figure 2, experimental airloads are well-predicted by CFD. As observed in Fig. 2(a), both the inviscid and viscous treatment of the wind tunnel wall yield accurate predictions of the outboard normal force, but the predictions deviate near the wall. It is an artifact of the existing uncertainties in the treatment of the wind tunnel wall in the experiment due to the presence of wall slots to enable translation of mounted wing along stream direction. In discussing with experimentalists, further uncertainties are anticipated as the wing force measurements are found to be sensitive to the size of the introduced wall fence to avoid leakage of flow into the wall slot. Figure 2(b) shows the effect of varying fence diameters on normal force coefficients. The airloads computation includes the experimental apparatus blockage factor, $\beta = (1.0+\epsilon)^2, \epsilon = 3.2\%$ in freestream dynamic pressure, i.e. $q_\infty = q_\infty^{CFD}/\beta$. This validates the computational solver and the assumptions made in the simulation set up.

E. Wing-Vortex Interaction

This section investigates the vortex wake interaction with the wing and consequently its effect on the wing loading. Several vortex strength values were considered. Further, several relative positions of VG with respect to wing are considered to provide insights onto interaction of VG vortex with wing tip vortex and its effect on the wing loading.

Direct hit Case

For this case, the wing angle of attack was held at 7 degrees, and VG angle of attack (α_{vg}) was set to 4 degrees. The VG tip height was placed such that it aligned with the wing for a direct wing vortex interaction, i.e. $\Delta Z = 0$ inch, Z

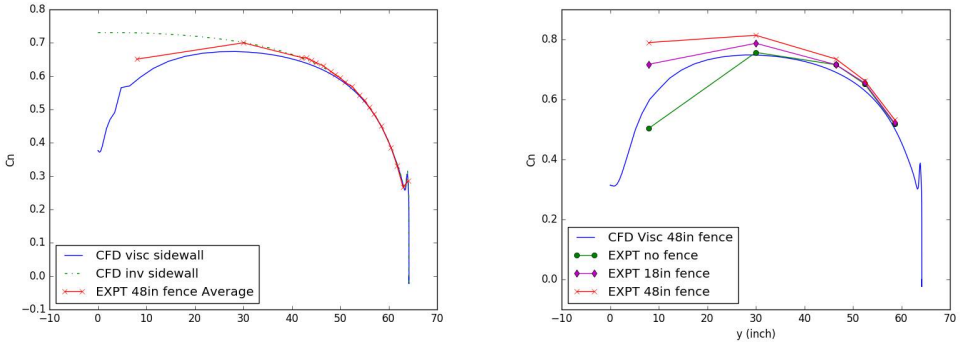

(a) Viscous vs inviscid $\alpha_w = 7°$ (b) Fence effect $\alpha_w = 8°$

Figure 2. Wing airloads and wall fence effect

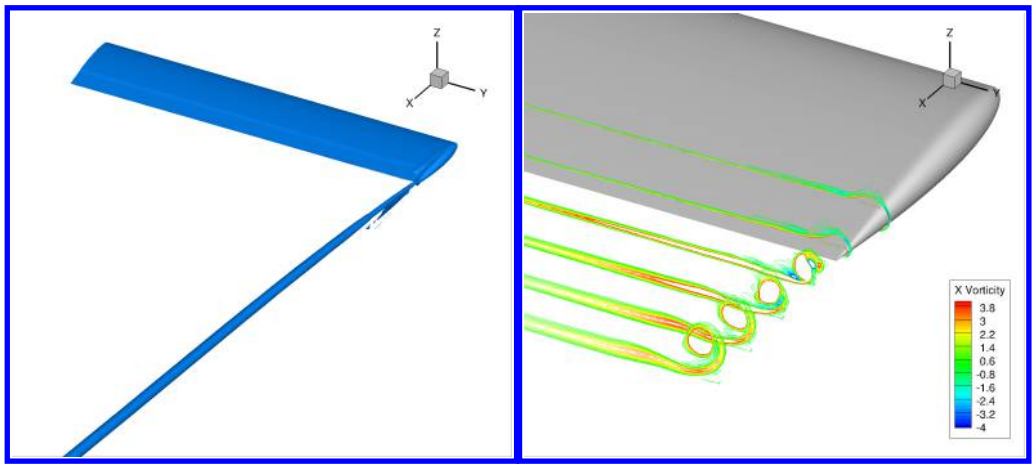

(a) Q-criterion (b) Vorticity contours

Figure 3. Solution for wing only case; $\alpha_w = 7°$

being the vertical separation distance between VG tip and wing quarter chord.

To ensure accurate resolution of the vortex, a vortex tracking grid (VTG) is used as shown in Figure 4(a).

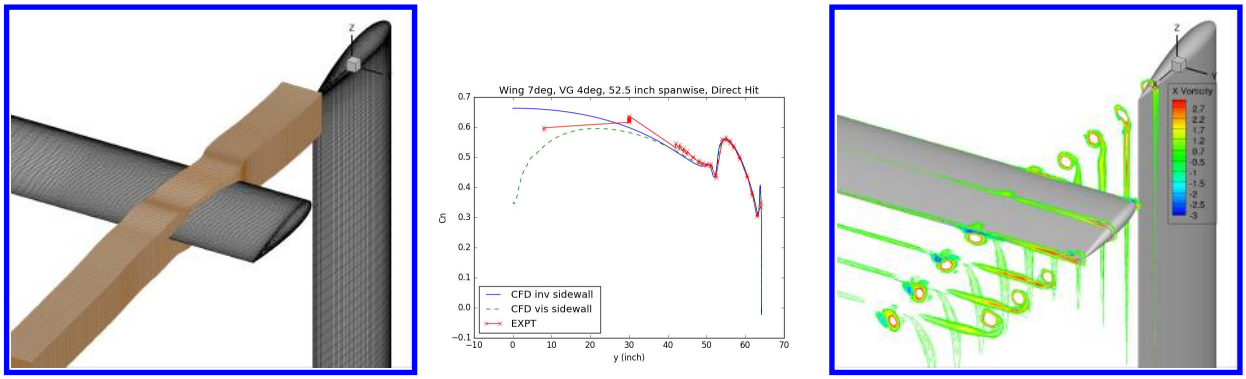

(a) Vortex Tracking Grid (b) Airloads (c) Vorticity contours

Figure 4. Solution with VG; $\alpha_w = 7°$, $\alpha_{vg} = 4°$, VG at 52.5in. span and $\Delta Z = 0.0$in.

Figures 4 indicates that the interaction between the wing and vortex is well-resolved for the VG with $\alpha_w = 7°$, $\alpha_{vg} = 4°$, VG at 52.5inch span and $\Delta Z = 0.0$inch, and the load on the wing was well-predicted. Vorticity magnitudes

in the streamwise direction for multiple planes in the downstream of the VG are plotted in Figure 4(c). As noted, the evolution of the VG tip vortex was well captured.

Another VG position, at 58.5 inch is considered at nominal direct hit vertical position. The solutions are shown in Figure 5. The vorticity magnitude in the stream wise direction on multiple planes in the downstream of the VG are plotted in 5(c). As noted in the figures, the roll-up is qualitatively similar to the experiments.

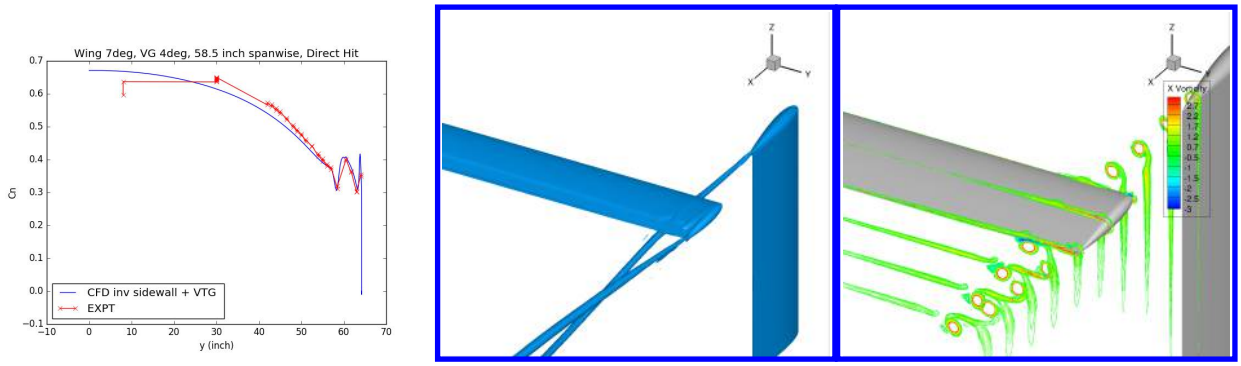

(a) Airloads (b) Q-criterion (c) Vorticity contours

Figure 5. Solution with VG; $\alpha_w = 7°$, $\alpha_{vg} = 4°$, VG at 58.5in. span and $\Delta Z = 0.0$in.

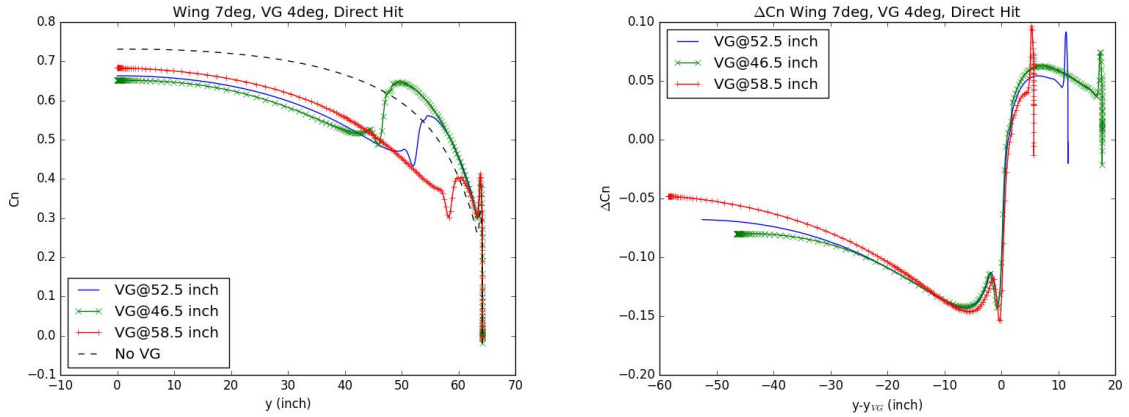

(a) Cn (b) ΔCn

Figure 6. Airloads for $\alpha_w = 7°$, $\alpha_{vg} = 4°$, VG at several locations and $\Delta Z = 0.0$in.

Figure 6 demonstrates the effect of vortex wake interaction on wing loading. As the vortex location moves inboard, the incremental airloads tend to be more symmetric compared to the vortex locations near the outboard of wing.

Figure 7 shows the solution from a stronger vortex wake interaction with wing. The VG is set at $\alpha_{vg} = 8°$ and placed at 46.5 inch at spanwise station. As noted in Figure 7(c), the direct interaction of vortex with wing results in complex vortex pair structures. The airloads predicted match well with the experimental values.

With increasing vertical separation of the vortex wake with respect to the wing, the vortex interaction is less complex as shown in Figure 8. However, secondary vortices are still introduced in VG vortex wake after interaction with the wing. The effect of vertical separation of VG vortex with wing is summarized in Figure 9. The figure shows that larger separation results in weaker lift increments with respect to the isolated wing. Also, the normal load spike present near the vortex gradually becomes less severe than the direct hit case.

1. Low-fidelity Model Validation

Figure 10 shows that the low-fidelity model is highly effective in capturing the airloads for the isolated wing. Figures 11 show consistently good predictions of airloads by the panel method throughout the wing span, although there exist slight over-predictions near the vortex location. A similar trend is noticeable for the VG vertical sweep cases in

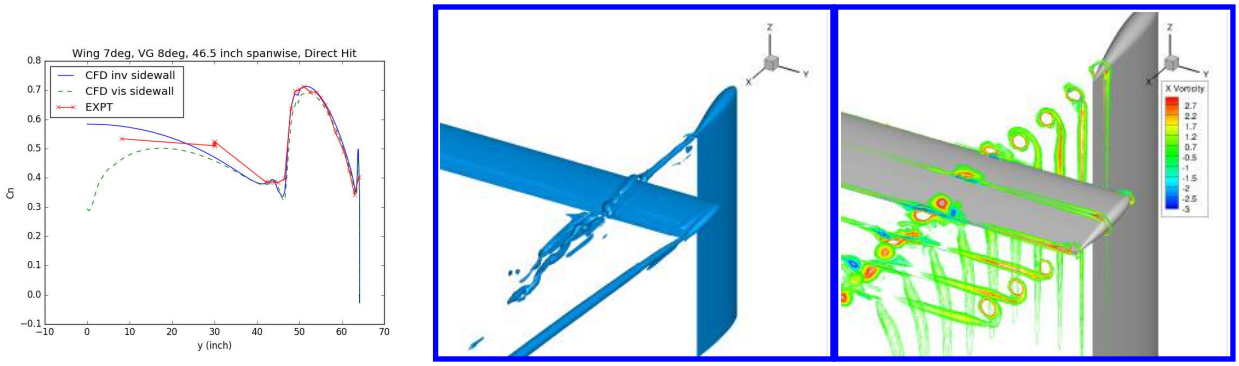

(a) Airloads (b) Q-criterion (c) Vorticity contours

Figure 7. Solution with VG; $\alpha_w = 7°$, $\alpha_{vg} = 8°$, VG at 46.5in. span and $\Delta Z = 0.0$in.

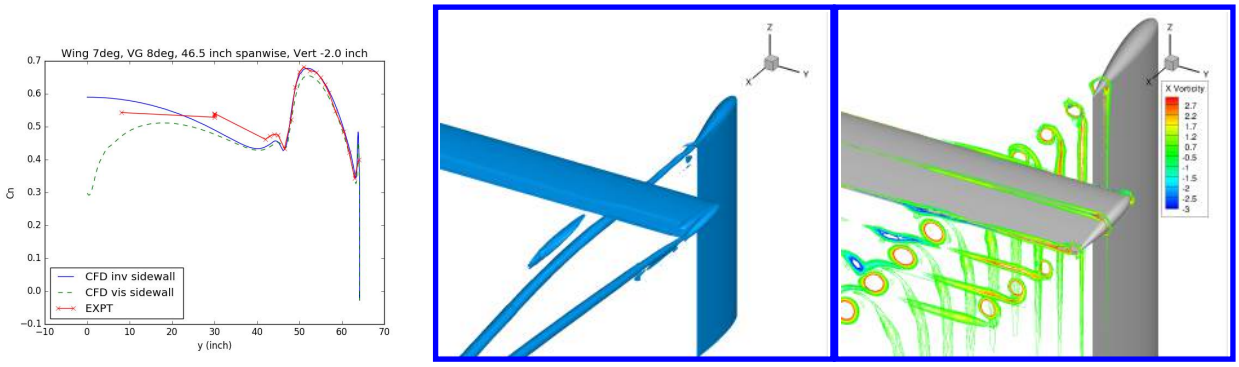

(a) Airloads (b) Q-criterion (c) Vorticity contours

Figure 8. Solution with VG; $\alpha_w = 7°$, $\alpha_{vg} = 8°$, VG at 46.5in. span and $\Delta Z = -2.0$in.

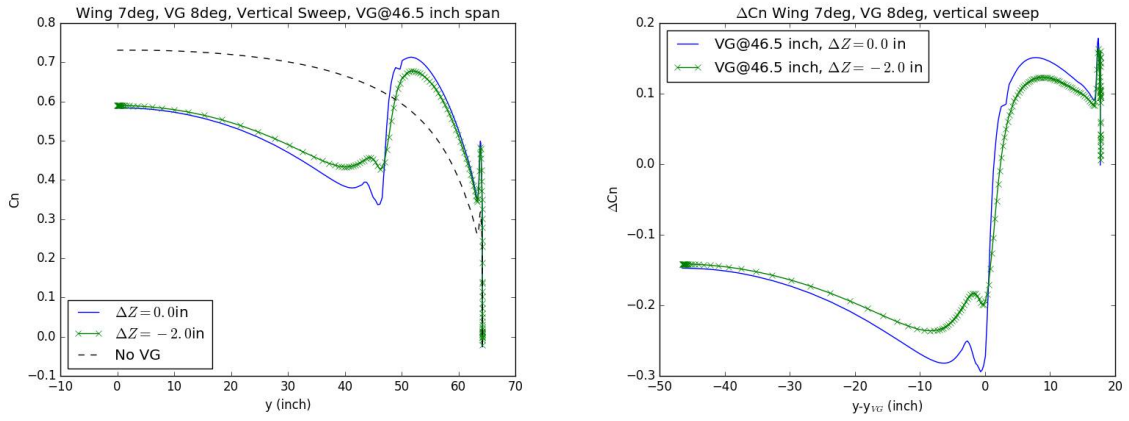

(a) Cn (b) ΔCn

Figure 9. Airloads for $\alpha_w = 7°$, $\alpha_{vg} = 8°$, VG at several vertical locations and $\Delta Z = 0.0$in.

Figures 12, in this case, with VG at larger $\alpha_{vg} = 8°$. The lift values are over-predicted again near the vortex, and the spanwise lift perturbation appears to be more gradual than that predicted by experiment and CFD. Overall, the low-fidelity model captures the essential aerodynamic loads very well.

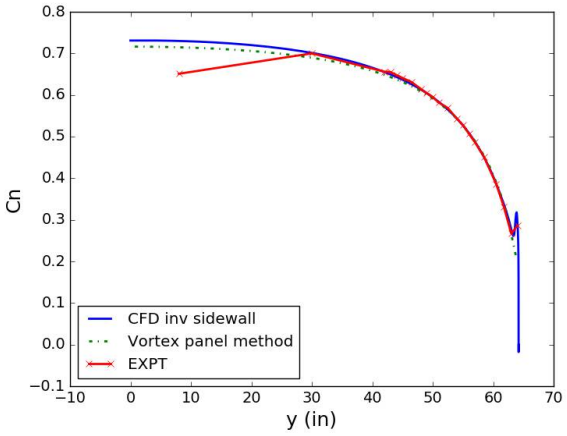

Figure 10. Validation of vortex panel method for wing only case; $\alpha_w = 7^\circ$

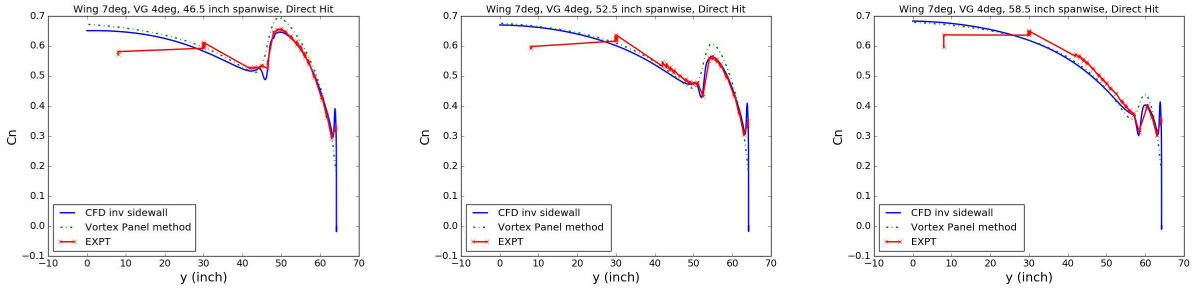

(a) VG at 46.5in (b) VG at 52.5in (c) VG at 58.5in

Figure 11. Validation of vortex panel method with VG direct hit; $\alpha_w = 7^\circ, \alpha_{vg} = 4^\circ$

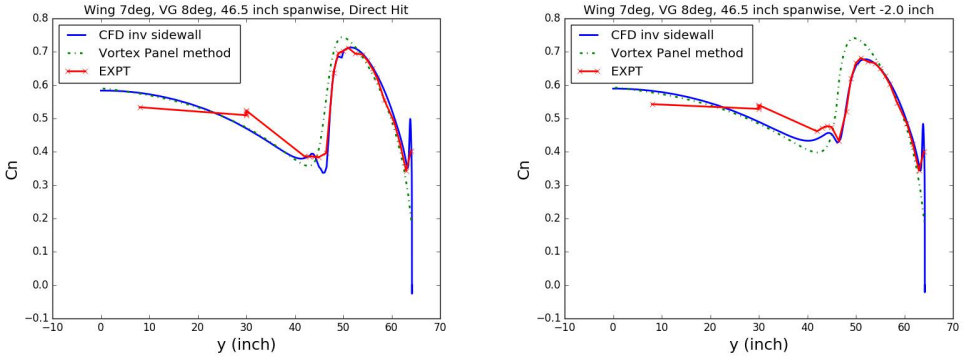

(a) VG at dz=0in (b) VG at dz=-2in

Figure 12. Validation of vortex panel method with VG vertical sweep; $\alpha_w = 7^\circ, \alpha_{vg} = 8^\circ$

F. Surface Pressure Validation

Figure 13 compare the predicted surface pressure by the CFD with the experimental values for the VG placed at 46.5 spanwise station at a nominal direct hit vertical position with $\alpha_{vg} = 4^\circ$. The measurements are well-predicted by CFD. It should be mentioned here that the CFD pressure prediction incorporates a pressure coefficient correction factor of $\Delta C_p \sim -0.25$ owing to the free stream pressure correction due to blockage effect. The figure also demonstrates the airload increments due to the vortex. The upwash due to the vortex at its outboard stations results in larger sectional

normal forces. Similarly, the downwash at the inboard stations of the vortex results in smaller values of sectional normal forces. The computational values correlate well with the experiment.

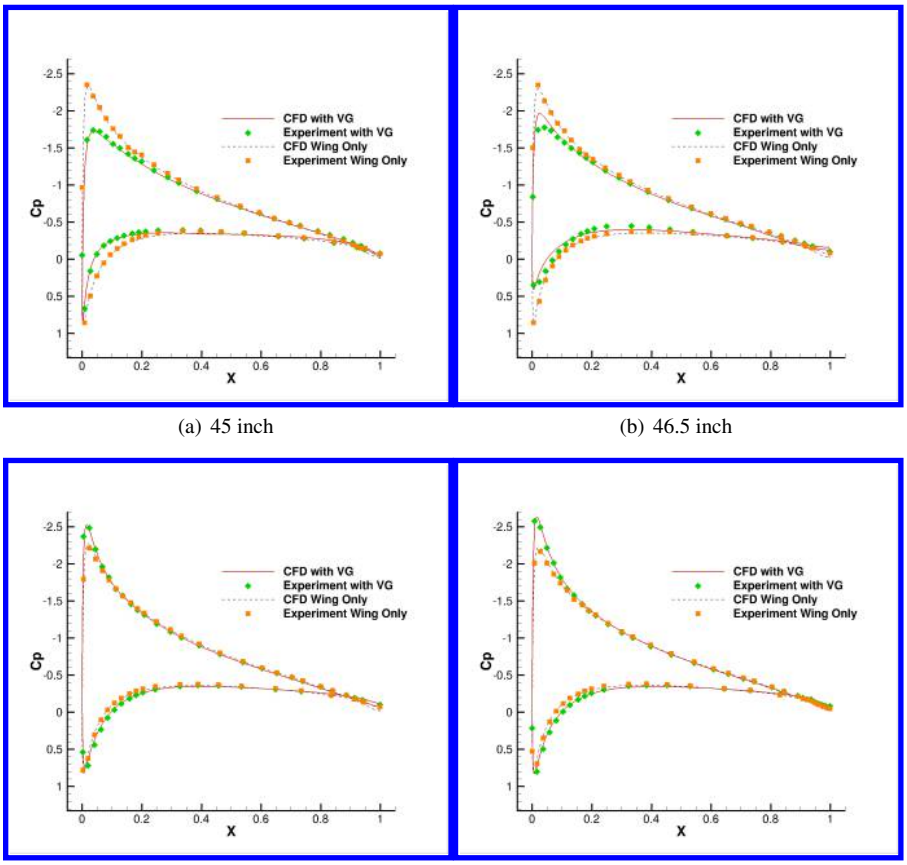

(a) 45 inch (b) 46.5 inch

(c) 48 inch (d) 49 inch

Figure 13. Surface pressure predictions for $\alpha_{vg} = 4°$, $\Delta Z = 0$in and VG at 46.5 in span

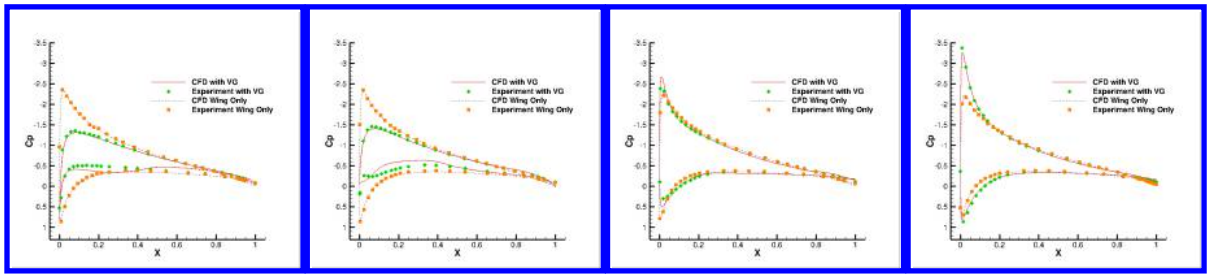

(a) 45 inch (b) 46.5 inch (c) 48 inch (d) 49 inch

Figure 14. Surface pressure predictions for $\alpha_{vg} = 8°$, $\Delta Z = 0$in and VG at 46.5 in span

Similar sectional pressure plots are presented for the stronger vortex strength, i.e. $\alpha_{vg} = 8°$, but VG corresponding to a direct hit and at the same spanwise station of 46.5 inch. The increments in normal load is more pronounced due to stronger vortex. This is evident when pressure values at the 49 in span sections for weaker and stronger vortex cases are compared – see figures 13(d) and 14(d). However, once the vortex is moved vertically 2 inches below the wing, the incremental normal load changes are weaker, as noted in Figures 15, especially Figure 15(d). The sectional pressure plots follow the same general trend as the other two cases, i.e. positive increment on normal load outboard of the vortex and decrement on normal load inboard of vortex.

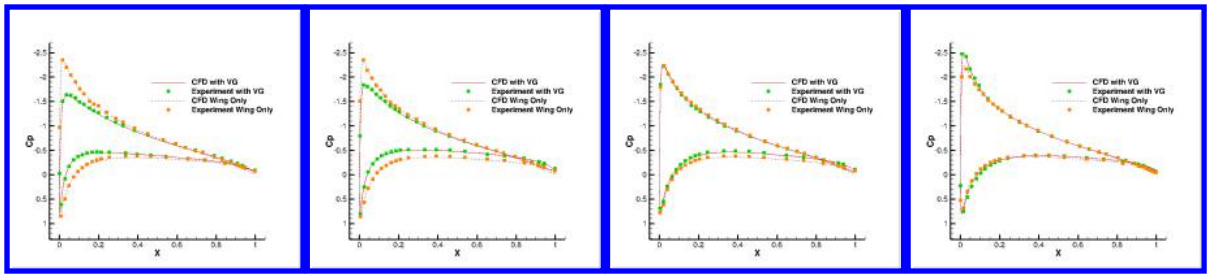

(a) 45 inch (b) 46.5 inch (c) 48 inch (d) 49 inch

Figure 15. Surface pressure predictions for $\alpha_{vg} = 8°$, $\Delta Z = -2$in and VG at 46.5 in span

G. Evolution of Vortices

Figure 16 compares the predicted vortex contours for the isolated wing case with experiments. As observed in the figure, the values are qualitatively well-predicted by CFD. Figures 17, 18, 19 demonstrate the evolution of vortex interaction from wing and VG for a nominal direct hit case for a VG placed at 58.5 inch from the wind tunnel side wall (0.5 chord inboard of wing tip). This confirms with what was observed in Figure 5, which showed how the wing tip vortex interacts with the vortex from VG and leads to a roll-up further downstream of the wake.

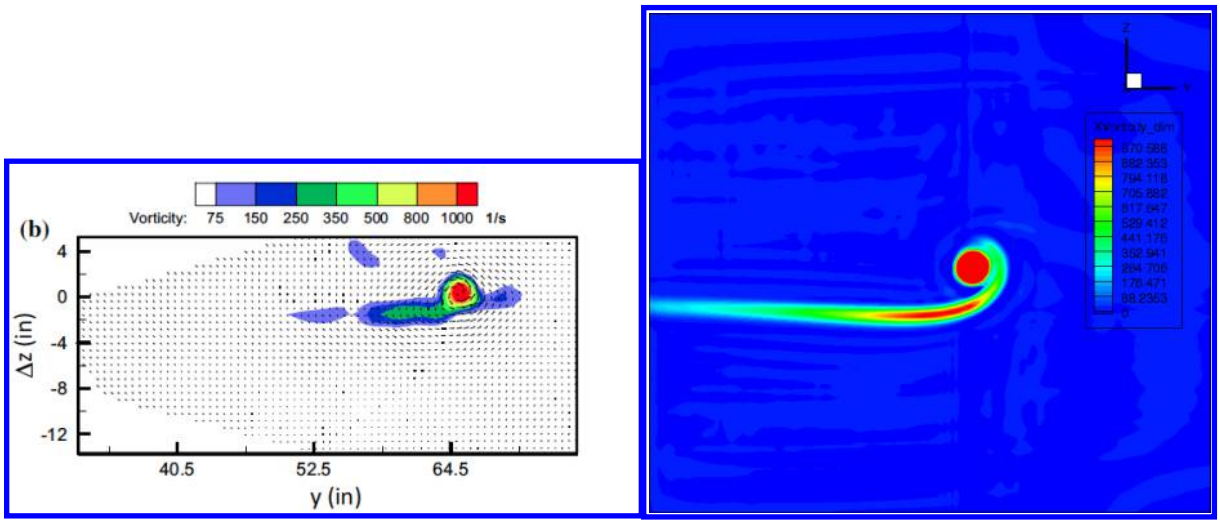

(a) Experiment [7] (b) CFD

Figure 16. Comparing wing only vortex strength at 4 ft behind wing TE for $\alpha_w = 7°$

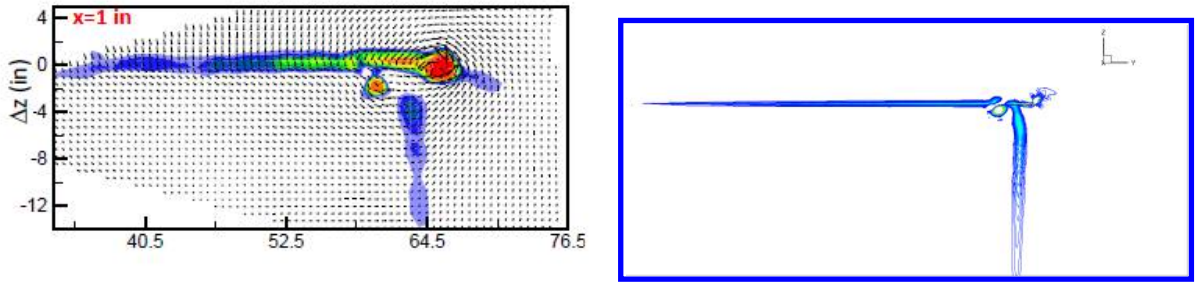

(a) Experiment (b) CFD

Figure 17. Wing and VG vortex interaction at 1 in behind wing TE for $\alpha_{vg} = 4°$, $\Delta Z = 0$.in. and VG at 58.5 in. span

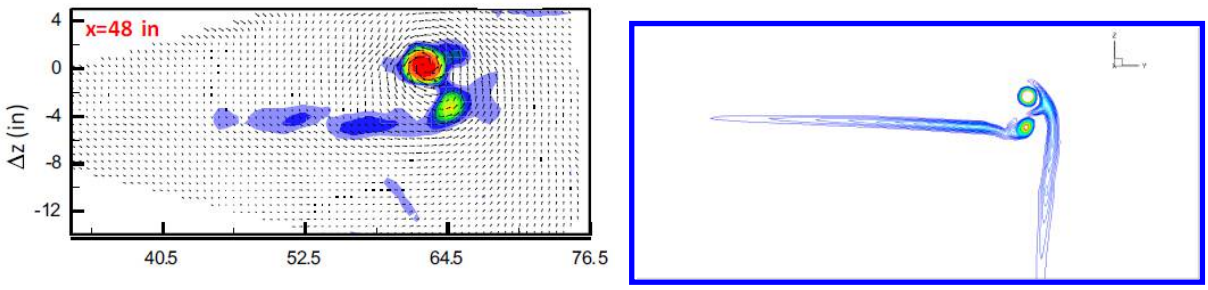

(a) Experiment (b) CFD

Figure 18. Wing and VG vortex interaction at 48 in behind wing TE for $\alpha_{vg} = 4°$, $\Delta Z = 0$.in. and VG at 58.5 in. span

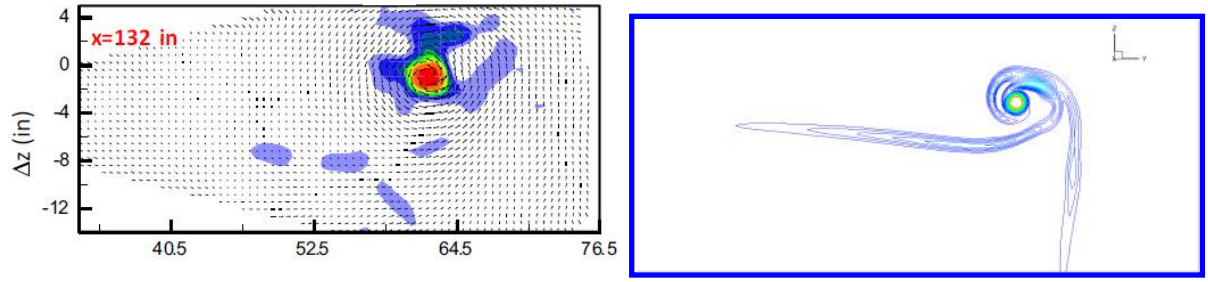

(a) Experiment (b) CFD

Figure 19. Wing and VG vortex interaction at 132 in behind wing TE for $\alpha_{vg} = 4°$, $\Delta Z = 0$.in and VG at 58.5 in. span

Shown in Figure 20, is the effect of vortex wake age on wing loading. It is observed that with the increasing distance of VG, the strength of VG gradually decreases resulting in weaker spike in normal load near the vortex.

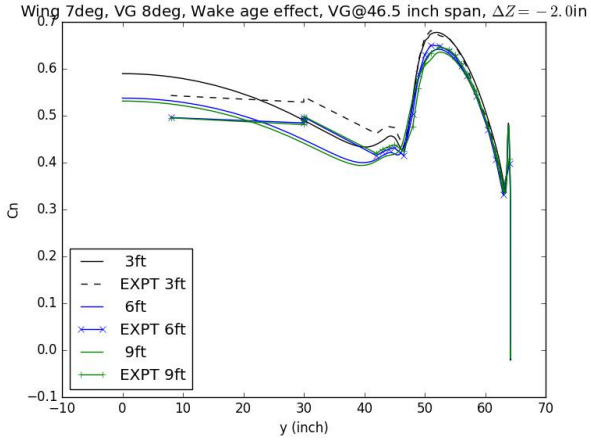

Figure 20. Vortex wake age effect: $\alpha_{vg} = 8°$, $\Delta Z = -2.0$in and VG at 46.5 in. span

IV. Propeller Wake-Wing Interaction

This section considers a more complex vortex interaction case of propeller wake with a wing, a typical flow situation encountered in turboprops and distributed propulsion systems. This particular case is more interesting because of the presence of large axial and swirl velocities due to the strong propeller tip vortices. The complex wake interaction on the wing has strong influence on its airloads.

The test case considered was experimentally investigated by Samuelsson [9, 10]. This work considers two specific

configurations from the experiment studies; one was, the isolated propeller and the second configuration was propeller with wing in its wake. There has been several computational studies in the past, including recent inviscid Euler computations by Thom et. al [26, 27]. The present work pursues more detailed RANS computations. The experimental flow conditions are summarized in Table 1.

Low-fidelity model details: The sectional lift coefficient slope $C_{l\alpha}$ was assumed to vary linearly between 1.5π to 1.7π, and zero-lift angle of attack was also assumed to vary linearly between 6.4 to 1 degrees from the root to the tip according to the approximated airfoil data found on online database. It is noted that accurate 2D CFD simulations for each section may improve the estimations.

Table 1. Propeller Conditions

J (M_{tip})	0.7 (0.655)
C_T	0.23
U_∞ (m/s) (M_∞)	50 (0.15)
Reynolds number (prop tip)	1.96×10^6
Reynolds number (wing)	1.70×10^6

A. Isolated Propeller Study

This section investigates the time averaged wake features in an isolated propeller. The propeller geometry, a typical medium sized turboprop commuter propeller geometry, is composed mainly of NACA 6 series airfoil section with varying thickness and twist along the span. The propeller radius is 0.64m. The detailed geometry description can be found in [9, 10, 26].

The mesh system of the propeller blade with nacelle geometry is as shown in Figure 21. The blade mesh is discretized with a C-O mesh system, with spanwise mesh sections collapsing near the propeller tip to resolve the tip section flow and vortex. Figure 21(a) shows how blade mesh is blended onto the nacelle geometry at its root. Its grid size is $149 \times 181 \times 56$ along the chordwise, spanwise and wall normal direction, respectively. The nacelle mesh, which captures the blade wake flow features, is composed of $175 \times 154 \times 400$ points along the azimuthal, nacelle wall normal and streamwise/nacelle-axis directions, respectively. Taking advantage of periodicity of the flow for a four bladed propeller, only one quadrant of rotor system is considered to save computational cost. Figures 21(b) and 21(c) show that the propeller wake region is well-resolved in the nacelle mesh. The outer boundary is approximately 10 propeller radii from nacelle and about 20 propeller radii downstream. The computation is performed in the rotor inertial reference frame while the nacelle rotates along the propeller.

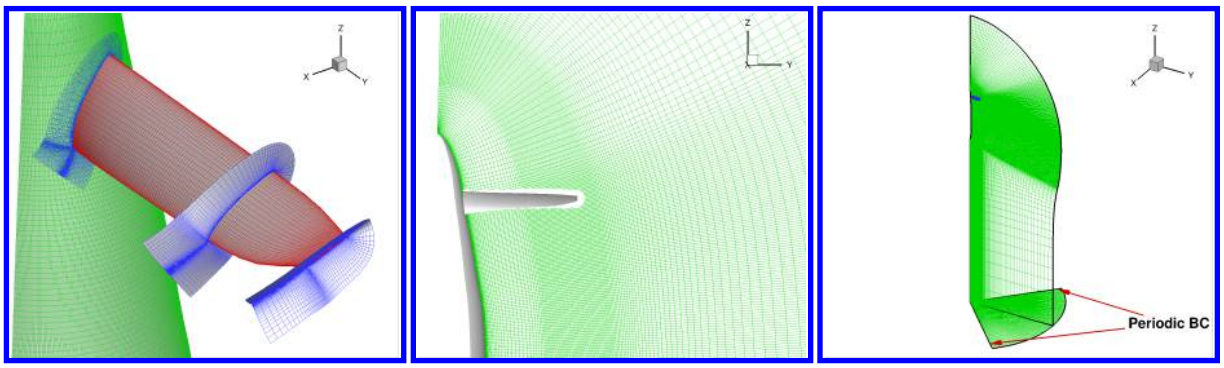

(a) Blended Blade mesh (b) Hole cut nacelle mesh (c) Full computational domain

Figure 21. Overset mesh system of isolated propeller configuration

The converged propeller performance predictions $[C_T, C_P] = [0.236, 0.240]$ compare well with the experimental values of $[C_{Texp}, C_{Pexp}] = [0.236, 0.230]$. Figure 22 show the vortex wake flow features of the propeller. Figure 22(a) reveals the quadruple helix structure with very slight contraction in its diameter as the vortices convect downstream of nacelle. Figure 22(b) shows the presence of 3D vortex sheets manifested along few azimuthal planes in propeller blade. Q-criterion isosurface reveal evolution of trailed vortex structures in Figure 22(c). Figure 23 compares the

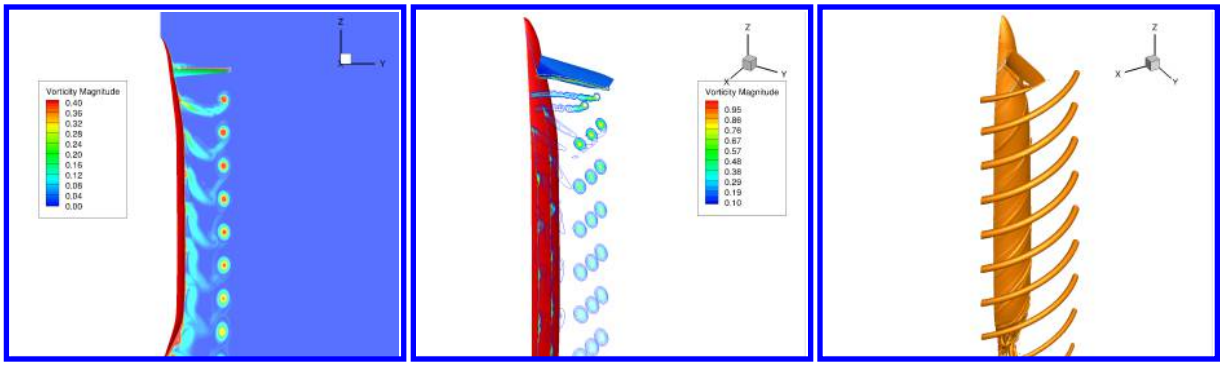

(a) Propeller wake (b) Wake 3D vortex sheets (c) Q-criterion isosurface

Figure 22. Wake solutions of the isolated propeller configuration

sectional lift coefficient among both models. Although there is a slight under-prediction of lift using vortex panel method, qualitatively the lift trend is well captured.

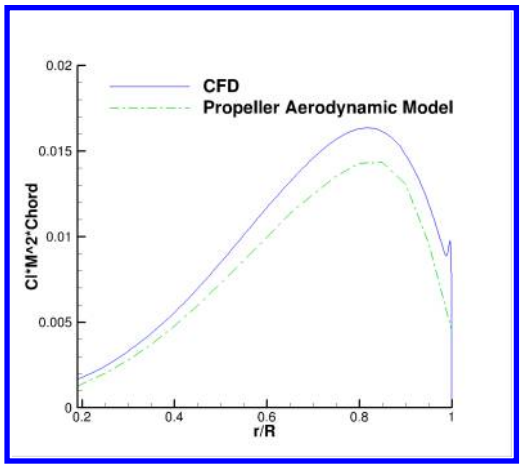

Figure 23. Sectional lift distribution on propeller

The predicted axial wake velocity at various planes downstream of propeller is compared with experimental values in Figure 24. It is observed that the propeller induces axial velocities as large as 170% or more of the free stream velocity (Figs. 24(c) and 24(c)). It is observed that the axial velocity values are under-predicted at planes closer to the propeller (Fig. reffig:isolatedpropVax1, but the discrepancies reduce at planes farther away from propeller. This could be due to the difference in geometry used for computation compared to the experimental geometry. The figures also show the predictions of the axial velocity by the propeller aerodynamic model. While consistent over-prediction is noticeable in all the vertical planes, the predictions are better in planes near the blade.

Figures 25 compare the swirl angles at the mentioned planes downstream of the propeller [a]. While the predicted swirl angles compare reasonably well with experimental values at most of the stations, the predictions at farther downstream planes are better. Large swirl angle values as large as 20° (Fig. 25(a) are observed near the root which gradually decay to zero values towards the tip as expected. The maximum swirl angle gradually reduces at planes farther away downstream of the propeller. In the figures, the predictions by the propeller aerodynamic model are also included. In contrast to the axial velocity predictions, the swirl angle values are consistently under-predicted in all the stations. Swirl angles are well-predicted at planes away from rotor plane.

B. Propeller Wake-Wing Interaction

The propeller wake interaction with the mounted wing on nacelle is considered in this section. The wing is mounted downstream of the propeller (0.174m below nacelle leading edge). It has a constant NACA$63_{(010)}A012$ airfoil section

[a]Swirl angle is positive in the rotation direction of the propeller (positive z-axis)

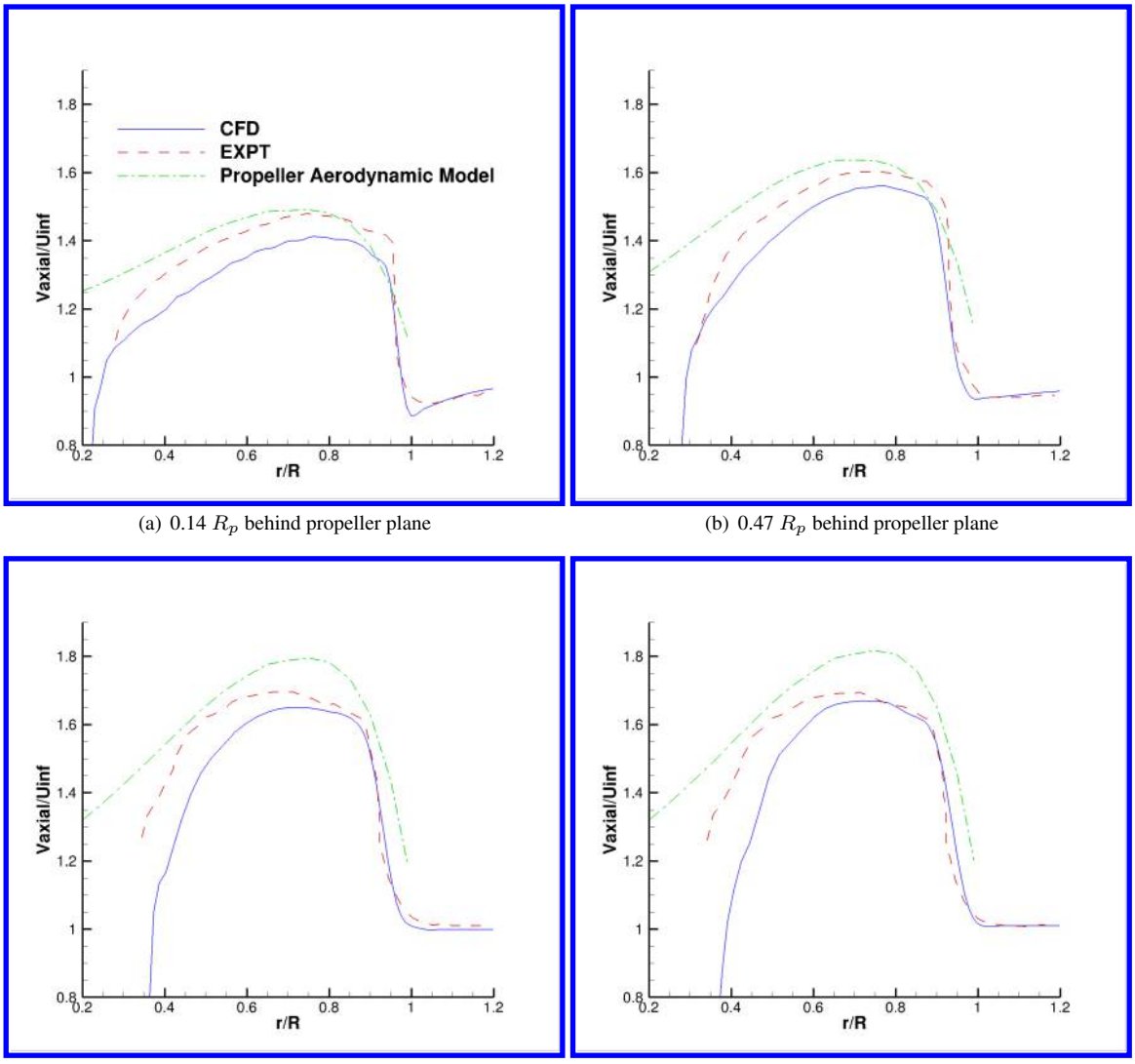

(a) 0.14 R_p behind propeller plane

(b) 0.47 R_p behind propeller plane

(c) 1.72 R_p behind propeller plane

(d) 3.0 R_p behind propeller plane

Figure 24. Axial velocity at several planes downstream of propeller

and spans 2.0m (a semi-span of 1.0m and aspect ratio of 2.0) in total. The details of the geometry can be found in [9].

Figure 26 summarizes the computational domain for the propeller-wing configuration. Because of the presence of wing, the whole rotor is considered instead of just the quadrant as considered for the isolated rotor case. In addition, the nacelle mesh system is split into two domains (Fig. 26(b)): a) an upper domain oversets propeller blades mesh system which rotates along with the propeller and b) the lower domain that remains static and resolves vortex wake trailed from the upper nacelle mesh. The information transfer across the two nacelle domains is achieved by incorporating a sliding boundary condition at the interface. The periodic boundary condition is still applied on both the nacelle meshes.

The complex flow features of the propeller vortex wake interaction with the wing is shown in Figures 27. Although the diameter of the helical vortex system contracts slightly downstream of propeller, it tends to grow downstream of the wing after the complex interaction. The vortex wake is found to disintegrate and grow weaker downstream of the wing after the interaction. Figure 27(c) further show the $4/rev$ wing lift history, as expected from a 4-bladed propeller wake aerodynamics. The lift history over ten revolutions also confirm that the solution is periodically converged. Pressure data is well-predicted by the computational model as shown in Figure 28. The figure validates the predicted pressure coefficient values at several spanwise stations of the wing. The plots also show the pressure fluctuations over one rotor revolution and as expected the fluctuations are the largest near $r/Rp = 0.95$ where the propeller trailed vortex wake directly interacts with the wing.

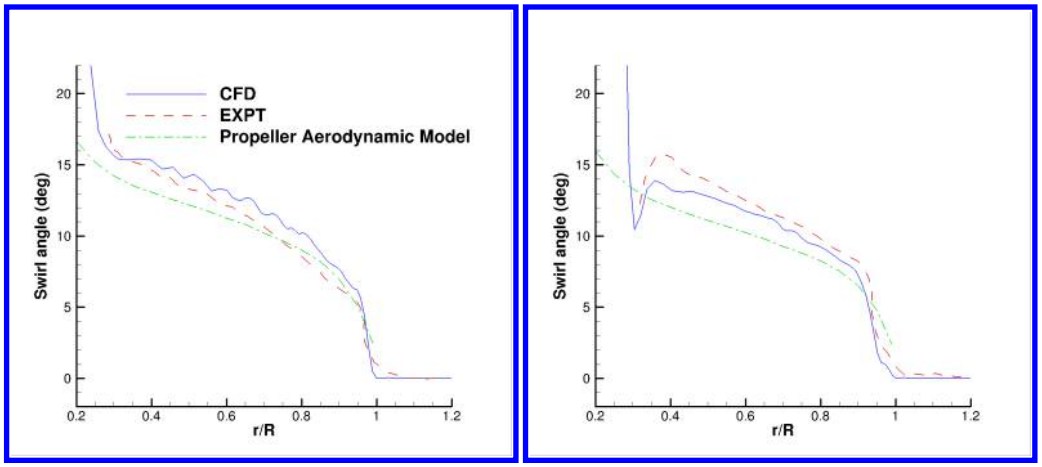

(a) 0.14 R_p behind propeller plane (b) 0.47 R_p behind propeller plane

(c) 1.72 R_p behind propeller plane (d) 3.0 R_p behind propeller plane

Figure 25. Swirl angle at several planes downstream of propeller

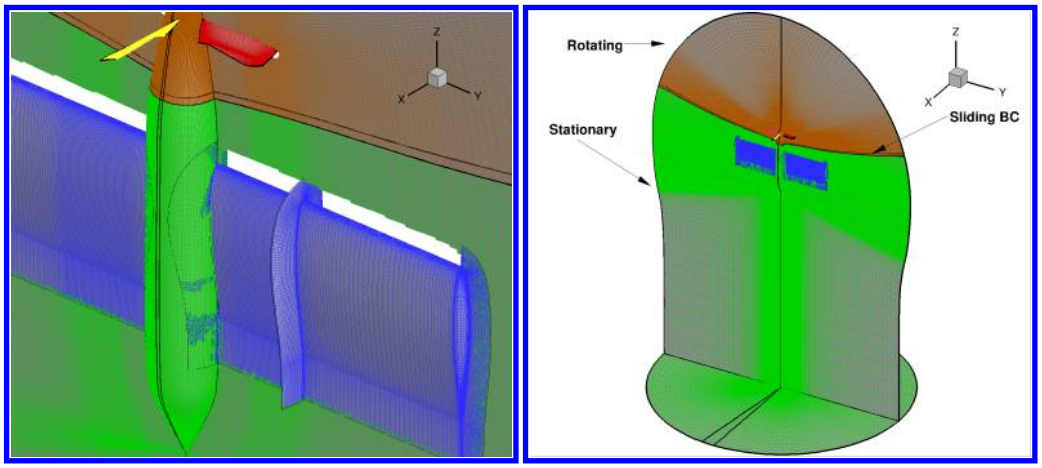

(a) Blended Wing mesh and hole cut (b) Full computational domain

Figure 26. Overset mesh system of the propeller-wing configuration

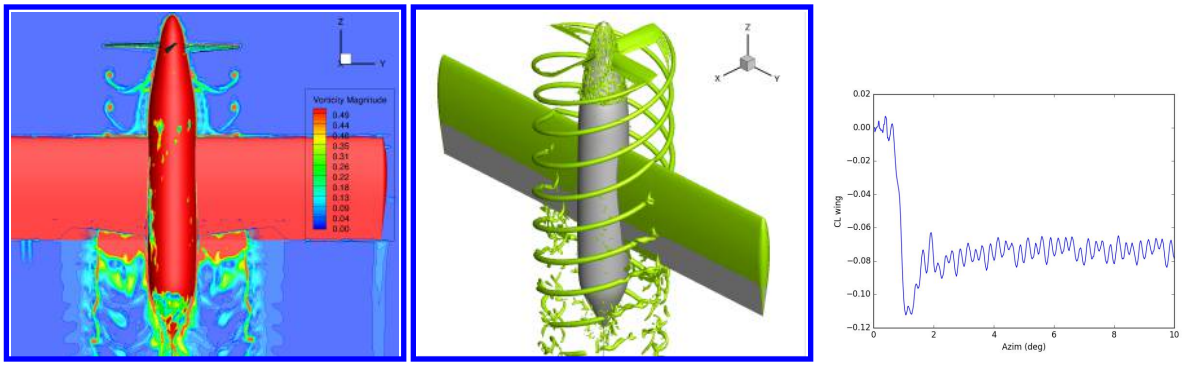

(a) Propeller wake (b) Q-criterion isosurface (c) Wing CL

Figure 27. Wake solutions of the propeller-wing configuration

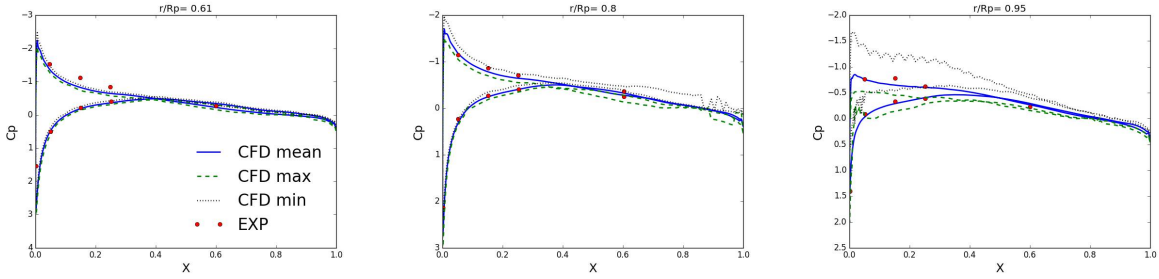

(a) r/Rp=0.61 (b) r/Rp=0.80 (c) r/Rp=0.95

Figure 28. Wing Cp at several spanwise stations

V. Summary

In this work, the interaction of vortices with lifting surfaces was studied using a two levels of modeling fidelity. A RANS-based CFD solver was chosen as the high-fidelity model and a novel vortex panel method, in conjunction with an extended blade element momentum theory, was used as the low-fidelity model. Detailed validations were pursued against data from three main experimental studies. Key observations from the studies are summarized below.

Wing-vortex Interaction:

- The high-fidelity RANS-based model (HFM) was used to model the vortex generator, vortex evolution and interaction with a downstream wing. The HFM accurately predicts wing airloads, operating in an vortex wake of varying strengths. The predictions were found to be generally more accurate in the outboard sections and are found to deviate from experiment near the wind tunnel wall. Uncertainties can be expected due to presence of wing slot opening as well as the sensitivity of wing loading to flow fence size.
- The HFM accurately captured peak-to-peak values and the location of the incremental normal lift variation due to the presence of vortex. In addition, the vortex strength values, the specific physics of evolution and interaction of wing vortex with the incoming vortex (locations and relative positions of the vortices) and vortex wakeage effects on wing airloads were accurately predicted, including in the case where the vortex core directly impacted the wing surface.
- The HFM successfully predicted the experimental wing surface pressure data to significant accuracy for all the cases considered.
- The low-fidelity model provided reasonably accurate predictions of the wing airloads for wing alone case as well as for several horizontal and vertical locations of vortex wake with respect to the wing.

Isolated propeller:

- The HFM accurately captured the swirl angle values in the propeller wake, although the axial velocities were slightly under-predicted at planes closer to the propeller.
- The HFM accurately captured the quadruple helix structure with slight contraction of the propeller vortex wake.
- The low-fidelity propeller aerodynamic model predicted propeller lift distribution to a good degree of accuracy. The axial velocity was slightly over-predicted and swirl angles were consistently under-predicted.

Wing mounted propeller:

- The helical wake vortex structure showed slight contraction before expanding upon its interaction with the wing in its wake and ultimately disintegrating downstream of the wing.
- The mean wing surface pressure was accurately predicted at several spanwise stations.

Qualitatively, the low-fidelity model captured the flow features, and propeller/wing performance trends very well, although quantitative discrepancies were noticeable in comparison to the CFD and experiment. The low-fidelity vortex panel method can be further improved using additional physical calibrations and can be a highly efficient tool in studying vortex dominated flow problems, at orders of magnitude less computational cost compared to the high-fidelity models.

VI. Acknowledgments

This work was supported by NASA under the project "Generalized Trajectory Modeling and Prediction for Unmanned Aircraft Systems" (Technical Monitor: Sarah Dsouza).

References

[1] Clarke, S., Lin, Y., Papathakis, K., and Samuel, A., "LEAPTech HEIST power architecture and testing," 2015.

[2] Rothhaar, P. M., Murphy, P. C., Bacon, B. J., Gregory, I. M., Grauer, J. A., Busan, R. C., and Croom, M. A., "NASA Langley Distributed Propulsion VTOL TiltWing Aircraft Testing, Modeling, Simulation, Control, and Flight Test Development," *14th AIAA Aviation Technology, Integration, and Operations Conference*, 2014, p. 2999.

[3] Ham, N. D., "Some conclusions from an inverstigation of blade-vortex interaction," *Journal of the American Helicopter Society*, Vol. 20, No. 4, 1975, pp. 26–31.

[4] K.S., W. and J., D. W., "Effects of perpendicular blade-vortex interaction, part 1: Turbulence structure and development," *AIAA Journal*, Vol. 37, No. 7, 1999, pp. 805–812.

[5] K.S., W., J., D. W., and Glegg, S. A., "Effects of perpendicular blade-vortex interaction, part 2: Parametric Study," *AIAA Journal*, Vol. 37, No. 7, 1999, pp. 813–817.

[6] Komerath, N. M., Smith, M. J., and Tung, C., "A review of rotor wake physics," *Journal of the American Helicopter Society*, Vol. 56, No. 2, 2011, pp. 022006–1–022006–19.

[7] Bhagwat, M. J., Caradonna, F. X., and Ramasamy, M., "Wing–vortex interaction: unraveling the flowfield of a hovering rotor," *Experiments in Fluids*, Vol. 56, No. 1, 2015, pp. 1–17.

[8] Ramasamy, M., Pete, A. E., Bhagwat, M. J., and Caradonna, F. X., "An experiment to simulate the airloads and wake typical of a hovering rotor," *American Helicopter Society Aeromechanics Specialists Conference*, San Fransisco, CA, 2014.

[9] Samuelsson, I., "Low speed wind tunnel investigation of propeller slipstream aerodynamic effects on different nacelle/wing combinations. Part 1," Tech. rep., Aeronautical Research Institute of Sweden, Stockholm. Aerodynamics Dept., 1987.

[10] Samuelsson, I., "Low speed wind tunnel investigation of propeller slipstream aerodynamic effects on different nacelle/wing combinations. Part 2," Tech. rep., Aeronautical Research Institute of Sweden, Stockholm. Aerodynamics Dept., 1990.

[11] Duraisamy, K. and Baeder, J. D., "High resolution wake capturing methodology for hovering rotors," *Journal of the American Helicopter Society*, Vol. 52, No. 2, 2007, pp. 110–122.

[12] Aranake, A. C., Lakshminarayan, V. K., and Duraisamy, K., "Computational analysis of shrouded wind turbine configurations using a 3-dimensional RANS solver," *Renewable Energy*, Vol. 75, 2015, pp. 818–832.

[13] Duraisamy, K., Ramasamy, M., Baeder, J. D., and Leishman, J. G., "High-resolution computational and experimental study of rotary-wing tip vortex formation," *AIAA journal*, Vol. 45, No. 11, 2007, pp. 2593–2602.

[14] Aranake, A. and Duraisamy, K., "Aerodynamic optimization of shrouded wind turbines," *Wind Energy*, 2016.

[15] Spalart, P. R. and Almaras, S. R., "A One Equation Turbulence Model for Aerodynamics Flow," Tech. Rep. 1992-0439, American Institute of Aeronautics and Astronautics, 1992.

[16] Roe, P. L., "Approximate Riemann solvers, parameter vectors, and difference schemes," *Journal of computational physics*, Vol. 43, No. 2, 1981, pp. 357–372.

[17] Lee, Y. and Baeder, J. D., "Implicit Hole Cutting — A New Approach to Overset Grid Connectivity," *16th AIAA Computational Fluid Dynamics Conference*, Washington, DC, June 2003.

[18] Lakshminarayan, V. K., *Computational Investigation of Microscale Coaxial Rotor Aerodynamics in Hover*, Ph. d. thesis, University of Maryland, 2009.

[19] Mishra, A. and Baeder, J. D., "Coupled Aeroelastic Prediction of the Effects of Leading-Edge Slat on Rotor Performance," *Journal of Aircraft*, Vol. 53, No. 1, 2015, pp. 141–157.

[20] Katz, J. and Plotkin, A., *Low-speed aerodynamics*, Vol. 13, Cambridge University Press, 2001.

[21] Leishman, J. G., *Principles of Helicopter Aerodynamics*, Cambridge University Press, 2002.

[22] Miranda, L. and Brennan, J., "Aerodynamic effects of wingtip-mounted propellers and turbines," *4th Applied Aerodynamics Conference*, 1986, p. 1802.

[23] Metcalfe, M., "On the modelling of a fully-relaxed propeller slipstream," *21st Joint Propulsion Conference*, 1985, p. 1262.

[24] Bhagwat, M. J., Ramasamy, M., and Caradonna, F. X., "Fundamental Characterization of Spanwise Loading and Trailed Wake Vortices," Tech. rep., AMRDEC Redstone Arsenal United States, 2016.

[25] Betz, A., "Behaviour of vortex systems," Tech. rep., TM 713, NACA, 1933.

[26] Thom, A. D., *Analysis of vortex-lifting surface interactions*, Ph. d. thesis, University of Glasgow, 2011.

[27] Thom, A. and Duraisamy, K., "Computational Investigation of Unsteadiness in Propeller Wake–Wing Interactions," *Journal of Aircraft*, Vol. 50, No. 3, 2013, pp. 985–988.